crystals

MDPI

Article

Frequency Magnetically Tunable Terahertz Perfect Absorber Based on Graphene and Silica Layered Dielectric

Zhenyan Wei, Yannan Jiang * and Jiao Wang

Guangxi Key Laboratory of Wireless Wideband Communication & Signal Processing, Guilin 541004, China
* Correspondence: ynjiang@guet.edu.cn

Abstract: A frequency magnetically tunable perfect absorber based on graphene in the terahertz (THz) region is proposed. The performance is analysed using the 4 × 4 transfer matrix method, demonstrating that the perfect absorption frequency of the proposed absorber for a left-handed circularly polarized (LCP) wave can be dynamically tuned by varying the external static bias magnetic field in three frequency ranges (0.95–2.2 THz, 4.15–5.4 THz, and 7.3–8.55 THz). Due to the destructive interference of the reflected waves and the graphene-induced photonic band gap, the maximum absorption of the LCP wave can reach 99.91%. In addition, the proposed absorber can tolerate a wide range of incident angles for the LCP wave. This study may have great potential for various applications, such as detectors, sensors, and other optoelectronic devices in the THz region.

Keywords: perfect absorber; graphene; photonic crystals; frequency magnetically tunable

1. Introduction

Graphene is a two-dimensional honeycomb-like material with a single layer of carbon atoms [1]. It has been widely studied due to its unique electrical, mechanical, thermal, and optical properties [2,3]. In terms of electrical properties, the surface conductivity can be tuned, and then graphene can be used in tunable devices such as modulators [4], filters [5], and absorbers [6]. In particular, frequency-tunable absorbers have been extensively studied from the GHz to infrared frequency ranges due to their wide application in sensors and detectors [7–14]. In the THz frequency range (i.e., from 0.1 to 10 THz [15]), graphene supports strong surface plasmon polaritons [16] and has strong photon localization [17], which significantly enhances the interaction between THz waves and graphene and effectively improves the absorption. Therefore, graphene-based frequency-tunable THz absorbers have become a research hotspot.

Recently, graphene-based frequency-tunable metamaterial [18–23], metasurface [24–26], and photonic crystal [27–29] THz absorbers have achieved tunable high-performance in narrowband, multiband, and broadband absorption. For many applications, frequency-tunable narrowband absorbers are preferred to broadband absorbers because they can absorb a given frequency without affecting adjacent frequencies. These THz absorbers can be frequency tuned by using a static bias electric field. However, the tunable frequency range of a frequency-tunable narrowband THz perfect absorber is limited (<3 THz) [19,23,27]. Although the tunable frequency range of the multiband THz perfect absorber based on the patterned graphene sandwich structure is broader, the multiple perfect absorption bands cannot be independently tuned [20,21,24]. To achieve independent tuning in a multiband THz absorber, a multilayer patterned graphene structure is designed, and different voltages are applied to each layer, which requires more electrodes to be added, thus increasing the fabrication and operation difficulties [18]. In addition, tunable absorption performance can also be achieved with an external static bias magnetic field (SBMF) [17,30–34], which reduces the fabrication difficulty due to the absence of electrodes. Cheng et al. [31] achieved tuning of the absorption frequency over a wide range. However, the tunable absorption was far from perfect absorption.

check for updates

Citation: Wei, Z.; Jiang, Y.; Wang, J. Frequency Magnetically Tunable Terahertz Perfect Absorber Based on Graphene and Silica Layered Dielectric. *Crystals* **2023**, *13*, 553. https://doi.org/10.3390/cryst13040553

Academic Editor: Alessandro Chiasera

Received: 16 February 2023
Revised: 17 March 2023
Accepted: 18 March 2023
Published: 23 March 2023

Copyright: © 2023 by the authors. Licensee MDPI, Basel, Switzerland. This article is an open access article distributed under the terms and conditions of the Creative Commons Attribution (CC BY) license (https://creativecommons.org/licenses/by/4.0/).

Rashidi et al. [32] and Mahesh et al. [34] achieved high absorption for a tunable frequency, but the tunable frequency range was limited. Therefore, achieving a graphene-based frequency magnetically tunable THz perfect absorber over a wide frequency range is still challenging.

In this paper, a frequency magnetically tunable THz perfect absorber based on graphene and SiO_2 layered structure is proposed. The absorption performance of the proposed absorber is tuned by varying the SBMF and investigated using the 4 $\times$ 4 transfer matrix method. The results show that the absorption ($\geq$99%) frequency for a left-handed circularly polarized (LCP) wave can be magnetically tuned in three frequency ranges (0.95–2.2 THz, 4.15–5.4 THz, and 7.3–8.55 THz), and the total tunable frequency range reaches 3.75 THz. Due to the destructive interference of the reflected waves and the graphene-induced photonic band gap, the maximum absorption of the LCP wave can reach 99.91%. In addition, the perfect absorption of the LCP wave at the absorption peak frequency does not significantly change with the incident angle when the incident angle is less than 40°.

2. Model and Method

2.1. Absorber and Magnetized Graphene Models

A side view of the proposed absorber model is shown in Figure 1a. The model can be described as $(DG)^N$, where D represents a nonmagnetic lossless dielectric (yellow), G represents graphene (black), and N represents the DG period number. The dielectric D and graphene G, with thicknesses of d_D and d_g and relative permittivities of ε_D and ε_g, are parallel to the x-y plane. The SBMF B is perpendicular to the graphene plane, so the surface conductivity of graphene can be described as a tensor that has not only diagonal terms σ_{xx} ($\sigma_{xx} = \sigma_{yy}$), but also off-diagonal terms σ_{xy} ($\sigma_{xy} = -\sigma_{yx}$). In the THz frequency range, the surface conductivity of highly doped graphene is often expressed by the Drude model. Specifically, σ_{xx} and σ_{xy} are, respectively, expressed as [35]

$$\sigma_{xx}(\omega, B) = \frac{W}{\pi} \frac{\tau^{-1} - i\omega}{\omega_c^2 - (\omega + i\tau^{-1})^2}, \tag{1}$$

and

$$\sigma_{xy}(\omega, B) = -\frac{W}{\pi} \frac{\omega_c}{\omega_c^2 - (\omega + i\tau^{-1})^2}, \tag{2}$$

where $W = e^2|E_F|/\hbar^2$ is the Drude weight, $\omega_c = eBv_F^2/E_F$ is the cyclotron angular frequency, and $\tau = \mu E_F/ev_F^2$ is the scattering time. e, E_F, $\hbar$, v_F, and μ are the electron charge, Fermi level, reduced Planck's constant, Fermi velocity, and carrier mobility, respectively. The relative permittivity of graphene can be written by a tensor $\overleftrightarrow{\varepsilon}_g$ as [36]

$$\overleftrightarrow{\varepsilon}_g = \begin{pmatrix} \varepsilon_{xx} & \varepsilon_{xy} & 0 \\ \varepsilon_{yx} & \varepsilon_{yy} & 0 \\ 0 & 0 & \varepsilon_{zz} \end{pmatrix}. \tag{3}$$

Here, $\varepsilon_{xx} = \varepsilon_{yy} = 1 + i\sigma_{xx}/\omega\varepsilon_0 d_g$, $\varepsilon_{xy} = -\varepsilon_{yx} = i\sigma_{xy}/\omega\varepsilon_0 d_g$, and $\varepsilon_{zz} = 1$, where ω, ε_0, and d_g are the operating angular frequency, vacuum permittivity, and thickness of graphene, respectively.

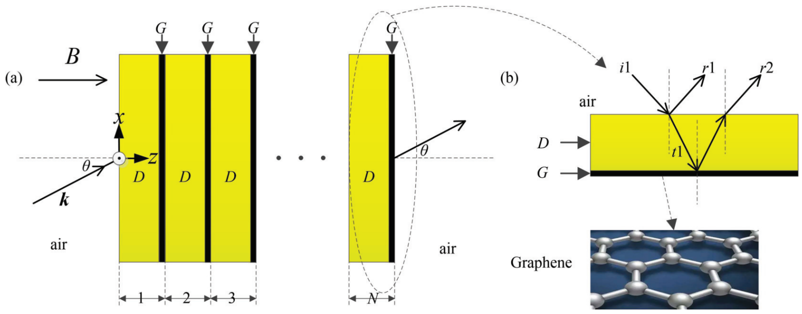

Figure 1. Schematics of the proposed absorber model. (**a**) $(DG)^N$ model and (**b**) $(DG)^1$ model.

2.2. Research Methods

The proposed absorber model consists of the layered isotropic dielectric D and monolayer magnetized graphene G. Therefore, the transmission and absorption performance of the proposed layered structures are analysed using the 4×4 transfer matrix method [37] and described in the following.

As shown in Figure 1a, the proposed absorber model is assumed to be placed in air. Therefore, the refractive indices of the incident wave space (the zeroth medium) and output wave space (the $(N+1)^{th}$ medium) are one, i.e., $n_{inc} = n_{out} = 1$. In addition, the THz wave is parallel to the x-z plane with angle of incidence θ and travels into the model at $z = 0$ and out of the model at $z = L_e$, i.e., L_e is the thickness of the proposed model. Hence, the tangential components of the wave vector $\boldsymbol{k}$ are $k_x = k_0 n_{inc} \sin\theta$ and $k_y = 0$, respectively, where k_0 is the free space wavenumber. For magnetized graphene, the longitudinal component of the wave vector $\boldsymbol{k}$ is $k_z = k_0\lambda_i$, where i = 1, 2, 3, and 4, and λ_i are four different z-components of the wave vector.

According to the Maxwell equations, on one side of monolayer anisotropic graphene, the tangential components of the electric field $\boldsymbol{E}$ and the magnetic field $\boldsymbol{H}$ can be expressed as [37,38]

$$\frac{\partial\psi(z)}{\partial z} = ik_0 \boldsymbol{A}_G \psi(z), \tag{4}$$

where

$$\psi(z) = \begin{pmatrix} e_x \\ e_y \\ h_x \\ h_y \end{pmatrix}, \tag{5}$$

$\boldsymbol{e} = \boldsymbol{E}/\sqrt{\eta_0}$ and $\boldsymbol{h} = \sqrt{\eta_0}\boldsymbol{H}$ are the normalized electric field and normalized magnetic field, respectively, and $\eta_0 = \sqrt{\mu_0/\varepsilon_0}$ is the impedance of free space. Moreover, $\boldsymbol{A}_G$ in Equation (4) can be expressed as [38]

$$\boldsymbol{A}_G = \begin{pmatrix} 0 & 0 & 0 & 1 - \frac{k_x^2}{k_0^2\varepsilon_{zz}} \\ 0 & 0 & -1 & 0 \\ -\varepsilon_{yx} & \frac{k_x^2}{k_0^2} - \varepsilon_{yy} & 0 & 0 \\ \varepsilon_{xx} & \varepsilon_{xy} & 0 & 0 \end{pmatrix}. \tag{6}$$

Therefore, the tangential components of the electric and magnetic fields on the other side of monolayer anisotropic graphene can be expressed as [37]

$$\psi(z + d_g) = \boldsymbol{M}_G(d_g)\psi(z), \tag{7}$$

where $\boldsymbol{M}_G(d_g)$ is the transfer matrix with 4×4 elements and can be written as

$$\boldsymbol{M}_G(d_g) = \boldsymbol{\Psi}_G \boldsymbol{P}_G(d_g)\boldsymbol{\Psi}_G^{-1}, \tag{8}$$

where $\boldsymbol{P}_G(d_g)$ is the diagonal propagation matrix and its four diagonal elements are $p_{ii} = exp(ik_0\lambda_i d_g)$. Moreover, $\boldsymbol{\Psi}_G$ is composed of eigenvectors of $\boldsymbol{A}_G$. They can be obtained from Equation (6) [39].

For the isotropic dielectric layer with a thickness of d_D, the transfer matrix $\boldsymbol{M}_D(d_D)$ can be similarly obtained from Equation (8). It is worth noting that $\varepsilon_{xy} = \varepsilon_{yx} = 0$ and $\varepsilon_{xx} = \varepsilon_{yy} = \varepsilon_{zz} = \varepsilon_D$; then, $\boldsymbol{A}_D$ can be accordingly simplified from Equation (6).

For the model shown in Figure 1a, the electric or magnetic fields at $z = 0$ and $z = L_e$ satisfy

$$\psi(z = 0) = (\boldsymbol{M}_G \boldsymbol{M}_D)^{-N}\psi(z = L_e), \tag{9}$$

Since a linearly polarized wave can be equivalent to two circularly polarized waves with equal amplitudes and opposite handedness, i.e., right-handed circularly polarized (RCP) and LCP waves, $\psi(z=0)$ and $\psi(z=L_e)$ can be expressed as [38]

$$\psi(z=0)=\boldsymbol{Q}^{(0)}\begin{pmatrix}a_R\\a_L\\r_R\\r_L\end{pmatrix},\psi(z=L_e)=\boldsymbol{Q}^{(0)}\begin{pmatrix}t_R\\t_L\\0\\0\end{pmatrix},\tag{10}$$

where

$$\boldsymbol{Q}^{(0)}=\frac{1}{\sqrt{2}}\begin{pmatrix}\cos\theta & \cos\theta & \cos\theta & \cos\theta\\ -i & i & i & -i\\ i\cos\theta & -i\cos\theta & i\cos\theta & -i\cos\theta\\ 1 & 1 & -1 & -1\end{pmatrix},\tag{11}$$

where $a_R(a_L)$, $r_R(r_L)$, and $t_R(t_L)$ are the amplitudes of incidence, reflection, and transmission of the RCP (LCP) wave, respectively. Hence, Equation (9) can be rewritten as

$$\begin{pmatrix}a_R\\a_L\\r_R\\r_L\end{pmatrix}=\boldsymbol{Q}^{(0)-1}(\boldsymbol{\Psi}_G\boldsymbol{P}_G\boldsymbol{\Psi}_G^{-1}\boldsymbol{\Psi}_D\boldsymbol{P}_D\boldsymbol{\Psi}_D^{-1})^{-N}\boldsymbol{Q}^{(0)}\begin{pmatrix}t_R\\t_L\\0\\0\end{pmatrix}=\boldsymbol{M}\begin{pmatrix}t_R\\t_L\\0\\0\end{pmatrix},\tag{12}$$

where $\boldsymbol{M}$ is the total transfer matrix, which connects the fields at $z=0$ and $z=L_e$; then, the transmission and reflection coefficients of co-polarization (with identical subscripts) and cross-polarization (with different subscripts) can be obtained as

$$\begin{aligned}
t_{RR}&=\frac{t_R}{a_R}\Big|_{a_L=0}=\frac{\boldsymbol{M}_{22}}{\boldsymbol{M}_{11}\boldsymbol{M}_{22}-\boldsymbol{M}_{12}\boldsymbol{M}_{21}},t_{LL}=\frac{t_L}{a_L}\Big|_{a_R=0}=\frac{\boldsymbol{M}_{11}}{\boldsymbol{M}_{11}\boldsymbol{M}_{22}-\boldsymbol{M}_{12}\boldsymbol{M}_{21}},\\
t_{LR}&=\frac{t_L}{a_R}\Big|_{a_L=0}=\frac{\boldsymbol{M}_{21}}{\boldsymbol{M}_{12}\boldsymbol{M}_{21}-\boldsymbol{M}_{11}\boldsymbol{M}_{22}},t_{RL}=\frac{t_R}{a_L}\Big|_{a_R=0}=\frac{\boldsymbol{M}_{12}}{\boldsymbol{M}_{12}\boldsymbol{M}_{21}-\boldsymbol{M}_{11}\boldsymbol{M}_{22}},\\
r_{RR}&=\frac{r_R}{a_R}\Big|_{a_L=0}=\frac{\boldsymbol{M}_{21}\boldsymbol{M}_{32}-\boldsymbol{M}_{22}\boldsymbol{M}_{31}}{\boldsymbol{M}_{12}\boldsymbol{M}_{21}-\boldsymbol{M}_{11}\boldsymbol{M}_{22}},r_{LL}=\frac{r_L}{a_L}\Big|_{a_R=0}=\frac{\boldsymbol{M}_{11}\boldsymbol{M}_{42}-\boldsymbol{M}_{12}\boldsymbol{M}_{41}}{\boldsymbol{M}_{11}\boldsymbol{M}_{22}-\boldsymbol{M}_{12}\boldsymbol{M}_{21}},\\
r_{LR}&=\frac{r_L}{a_R}\Big|_{a_L=0}=\frac{\boldsymbol{M}_{21}\boldsymbol{M}_{42}-\boldsymbol{M}_{22}\boldsymbol{M}_{41}}{\boldsymbol{M}_{12}\boldsymbol{M}_{21}-\boldsymbol{M}_{11}\boldsymbol{M}_{22}},r_{RL}=\frac{r_R}{a_L}\Big|_{a_R=0}=\frac{\boldsymbol{M}_{11}\boldsymbol{M}_{32}-\boldsymbol{M}_{12}\boldsymbol{M}_{31}}{\boldsymbol{M}_{11}\boldsymbol{M}_{22}-\boldsymbol{M}_{12}\boldsymbol{M}_{21}}.
\end{aligned}\tag{13}$$

3. Results and Discussion

In the investigation of the proposed $(DG)^N$ model, the centre frequency f_0 of the incident wave is 1.59 THz, and the angle of incidence θ is 0 (unless specifically mentioned in the following discussion). Furthermore, the dielectric D is set as SiO_2 with a refractive index n_D of 2.25 (lossless dielectric, i.e., extinction coefficient κ = 0) [40], whose optical thickness is a quarter wavelength, i.e., $n_Dd_D=\lambda_0/4$ ($\lambda_0=c/f_0$ is the centre wavelength, where c is the speed of light in vacuum), and $d_D=21$ µm. The parameters of graphene are $E_F=0.1$ eV, $v_F=10^6$ m s^{-1}, $\mu=10^5$ cm^2 V^{-1} s^{-1}, and $d_g=0.335$ nm [41]. It should be noted that the maximum magnetic field used in this paper (7 T) can be generated by a split-coil superconducting magnet [35].

3.1. Absorption for Various Period Numbers N

To obtain the perfect absorption performance of $(DG)^N$, the absorption of LCP and RCP waves for various N are shown in Figure 2a. The absorption of LCP and RCP waves is different due to the magnetic circular dichroism of graphene [42]. The absorption (A_L) of the LCP wave at the centre frequency is enhanced as N increases, and A_L = 99.91% when $N\geq 6$. However, the absorption (A_R) of the RCP wave is very slightly enhanced. For example, A_R is less than 5% when $N=8$. Therefore, the absorption performance of the proposed model for the LCP wave is mainly analysed in the following discussion.

The proposed model achieves near-unity absorption due to the destructive interference of the reflected waves [43] and the graphene-induced photonic band gap [44]. The destructive interference of the reflected waves is mainly due to the structure of DG. As shown in Figure 1b, the incident wave i_1 is incident from a dielectric with a low refractive index (i.e., air) to a dielectric with a high refractive index (i.e., the surface of D), which causes half-wave loss, meaning that the phase difference between the reflected wave r_1 and the incident wave i_1 is π. Subsequently, the refracted wave t_1 is incident into D. Due to the optical thickness of D being set as $\lambda/4$, the total optical path difference in D is $\lambda/2$ when $\theta = 0$, and the phase difference between r_2 and i_1 is π. In addition to the total optical path difference, the half-wave loss caused by t_1 from D to the surface of graphene G should also be considered, and the total phase difference between r_2 and i_1 is 2π. Therefore, the phase difference between r_1 and r_2 is π, and then, destructive interference occurs. To better illustrate the destructive interference in DG, the transmittance, reflectance, and absorption of G and DG for the LCP wave are shown in Figure 2b. At approximately f_0, R_{LL} is equal to zero, and R_{RL} is significantly depressed in DG, which means that the destructive interference of the reflected waves occurs. Therefore, the A_L in DG is further enhanced compared to G, while the transmittance T_{LL} in DG is nonzero, resulting in imperfect absorption. By increasing N, a graphene-induced photonic band gap (i.e., $T_{LL} = 0$, as shown in Figure 2c) can be formed so that A_L is closer to 100% and perfect absorption can be obtained. At approximately f_0, it can also be seen from Figure 2c and d that T_{LL} gradually approaches zero with increasing N, while R_{RL} is independent of N. Finally, $N = 6$ is chosen as the optimal period number of the proposed model, which has perfect absorption for the LCP wave.

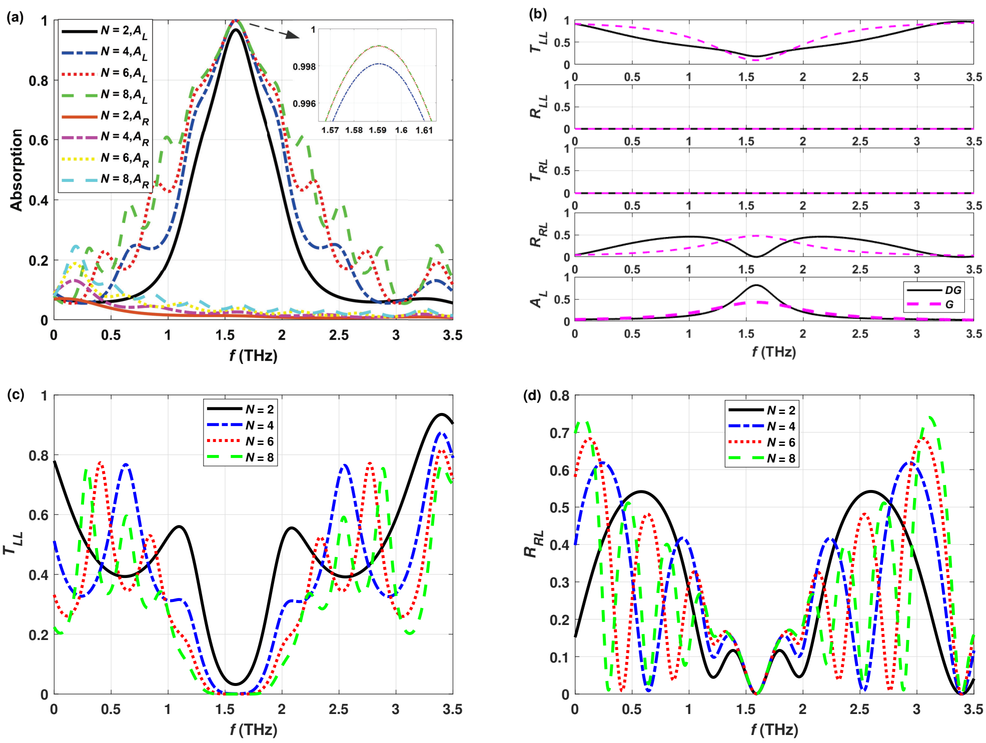

Figure 2. (**a**) Absorption (A_L and A_R), (**c**) transmittance (T_{LL}), and (**d**) reflectance (R_{RL}) of $(DG)^N$ with various N, and (**b**) reflectance, transmittance, and absorption of DG and G for the LCP wave, when B = 1 T.

To further understand the mechanism of perfect absorption for the LCP wave, the electric field amplitude distributions of the LCP and RCP waves are shown in Figure 3. The electric field of the LCP wave gradually decays and approaches zero at $z = L_e$, while the RCP wave propagates through $(DG)^6$ without attenuation. Therefore, only the LCP wave is perfectly absorbed.

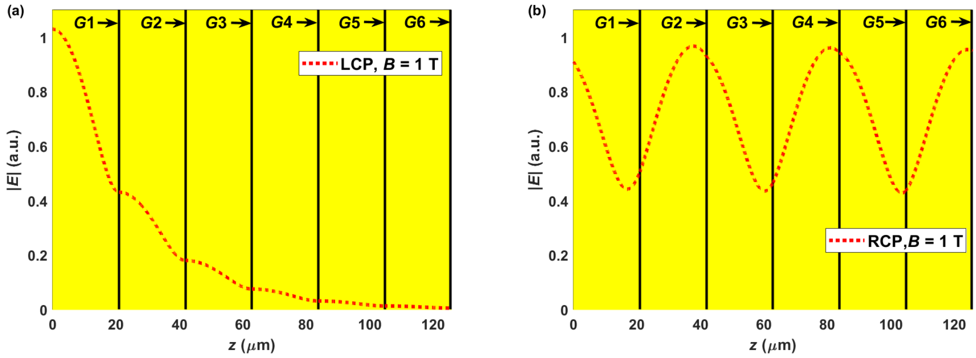

Figure 3. Electric field amplitude distributions of the (**a**) LCP and (**b**) RCP waves in $(DG)^6$ when $B = 1$ T.

3.2. Frequency Tuning with Various SBMFs B

The absorption peak frequency for the LCP wave can be tuned by varying the SBMF B, as shown in Figure 4a. The peak frequency of A_L is blueshifted while the peak value remains unchanged (i.e., $A_L = 99.91\%$ at 1.59, 4.77, and 7.95 THz) as B increases. To explain the mechanism of magnetic tuning of the absorption peak frequency, the imaginary part of the relative permittivity xx-component of graphene (i.e., Im(ε_{xx})) for $B = 1$, 3, and 5 T is plotted in Figure 4b. The peak frequency of Im(ε_{xx}) coincides with the absorption peak frequency in Figure 4a. Due to the presence of absorption and the lossless nature of the dielectric D, graphene must be lossy. Furthermore, Im(ε_{xx}) is usually used to represent ohmic loss [31]. Therefore, the maximum loss can occur at the peak frequency of Im(ε_{xx}), and then, the optimal absorption can also be achieved. In addition, it can be seen from Figure 4a that the peak frequencies of 4.77 and 7.95 THz are three and five times the peak frequency of 1.59 THz, respectively, and these increases are equal to the increases in the tuned B. This occurs because f_0 is set to be the cyclotron frequency f_c at $B = 1$ T, which is linearly related to B. Therefore, peak frequency magnetic tuning of A_L can be realized for $(DG)^6$.

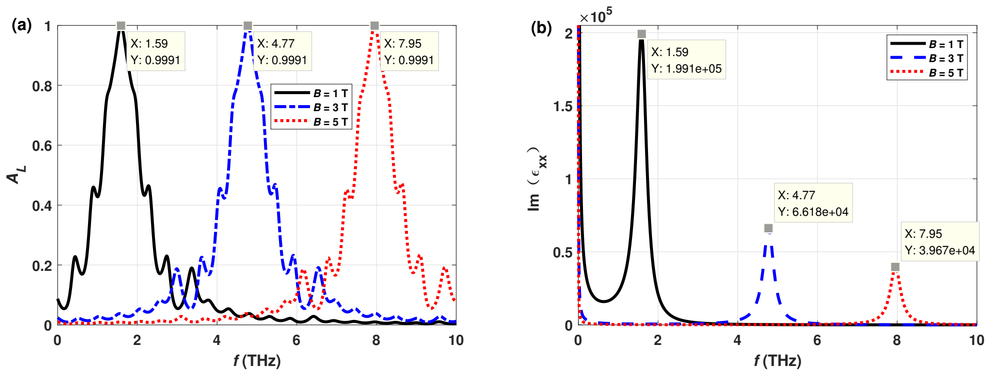

Figure 4. (**a**) Absorption of $(DG)^6$ for the LCP wave; (**b**) imaginary part of the relative permittivity xx-component of graphene for $B = 1$, 3, and 5 T.

The peak frequency of A_L for $(DG)^6$ with varying B is shown in Figure 5. Three frequency bands of the absorption peak with $A_L \geq 99\%$ appear in the investigated frequency range, which can be illustrated by the following formula:

$$f_p = \frac{c}{n_D d_D} \times \frac{l}{4}, \tag{14}$$

where f_p is the peak frequency, and l is a positive number. When the refractive index n_D and thickness d_D of the dielectric are fixed, f_p is mainly determined by l. Specifically, destructive interference, with minimum reflection and maximum absorption, can be achieved when l is an odd number. For example, it can be seen from Figure 5 that destructive interference can be achieved and A_L is maximum when $f_p = 4.76$ THz and $l = 3$. In contrast, constructive interference can be achieved and A_L is minimum when $f_p = 3.17$ THz and $l = 2$. Therefore, the frequency of $A_L \geq 99\%(90\%)$ for $(DG)^6$ is tuned by varying B in the frequency ranges of 0.95–2.2 THz, 4.15–5.4 THz, and 7.3–8.55 THz (0.63–2.53 THz, 3.8–5.7 THz, and 6.98–8.88 THz).

To demonstrate the advantage of the proposed absorber, we further compare it with other graphene-based frequency magnetically tunable absorbers reported in recent years. Table 1 illustrates the comparative results. From Table 1, we see that the proposed absorber has the widest tunable frequency range with the highest absorption, implying good performance. Therefore, the proposed absorber can be better used in circularly polarized wave sensors [32], circular polarizers [45], and MCD (the difference in the absorption of LCP and RCP waves induced by a magnetic field) photodetectors [34].

Table 1. Comparison with other graphene-based frequency magnetically tunable absorbers.

Reference	Absorption	Frequency Tunable Range (THz)	f_L (THz)	f_H (THz)
[17]	90%	0.2	4.24	4.44
[32]	90%	0.8	3.37	4.17
[33]	70%	1	0	1
[34]	95%	0.84	3.85	4.69
Present study	99%	3.75	0.95	8.55

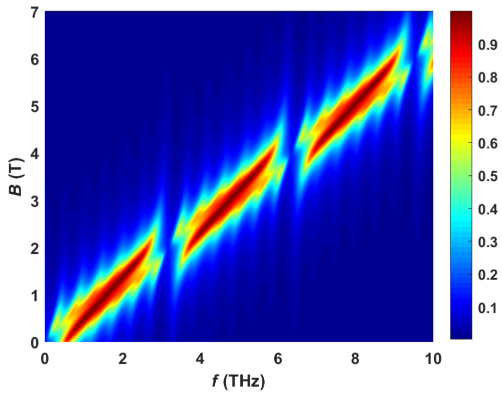

Figure 5. B-dependent absorption of the LCP wave for $(DG)^6$.

3.3. Influence of Incident Angle θ on Magnetic Tuning

The incident angle is highly related to the absorption performance [27–29]. Therefore, the magnetic tuning with various incident angles is investigated. The θ-dependence and B-dependence of A_L are shown in Figure 6. When the incident angle is less than 40°, the peak frequencies at B = 3 and 5 T exhibit a slight blueshift and the absorption is more than 99%, which is beneficial for the application of $(DG)^6$ in wide-angle frequency magnetically tunable absorbers. Here, the blueshift of the peak frequency is mainly due to the periodic structure of graphene and the dielectric. In addition, as the incident angle increases, the blueshift becomes more pronounced as the peak frequency increases [46].

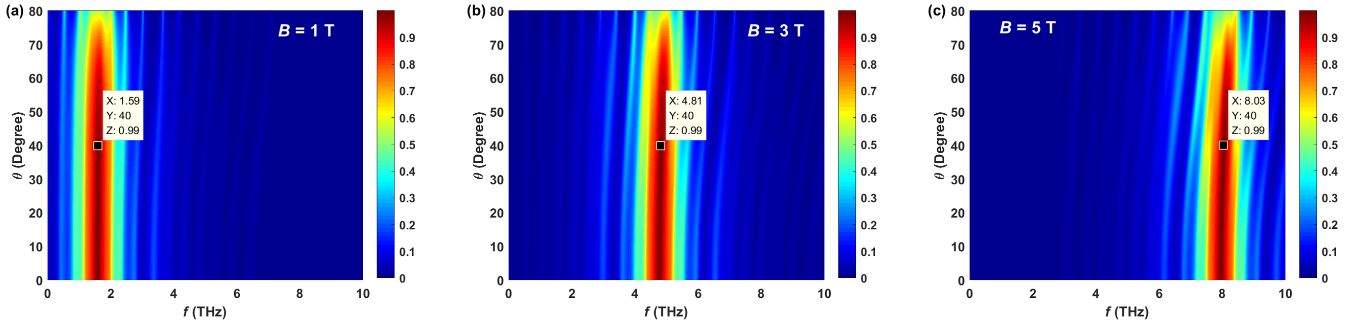

Figure 6. θ- and B-dependent absorption of the LCP wave for $(DG)^6$; (**a**) B = 1 T, (**b**) B = 3 T, and (**c**) B = 5 T.

3.4. Influence of the Nonmagnetic Dielectric Loss

Previous studies have discussed the magnetically tunable absorption performance of materials with the nonmagnetic dielectric SiO_2 as a lossless medium (i.e., extinction coefficient $\kappa_{\mathrm{sio}_2} = 0$). However, in practical manufacturing, SiO_2 has losses, and it is crucial to investigate the influence of its losses on the magnetically tunable absorption performance. The absorption of the proposed model ($(DG)^6$) with different extinction coefficients κ_{sio_2} is shown in Figure 7 for B = 1, 3, and 5 T. It can be seen from the figure that the loss of SiO_2 has almost no influence on the magnetically tunable absorption performance when $\kappa_{\mathrm{sio}_2} \leq 0.001$. However, when $\kappa_{\mathrm{sio}_2} > 0.001$, although the influence of SiO_2 loss on the absorption performance at the centre frequency is relatively small, it significantly affects the absorption performance outside the 1 THz bandwidth around the centre frequency. Therefore, in practical manufacturing, a nonmagnetic dielectric SiO_2 with an extinction coefficient $\kappa_{\mathrm{sio}_2} \leq 0.001$ should be selected to achieve more stable magnetically tunable absorption performance.

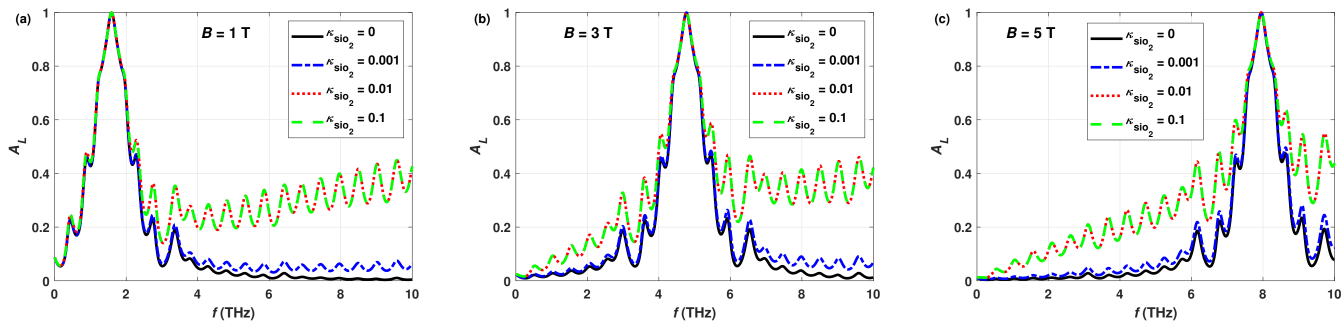

Figure 7. Absorption of the LCP wave for the proposed model $(DG)^6$ with various extinction coefficients: (**a**) B = 1 T, (**b**) B = 3 T, and (**c**) B = 5 T.

4. Conclusions

In this study, a frequency magnetically tunable THz perfect absorber based on graphene and silica layered structures is proposed. The absorption performance of the proposed absorber is investigated using the 4 × 4 transfer matrix method. The absorption ($\geq$99%) peak frequency for an LCP wave of the proposed model can be tuned by varying the SBMF in three frequency ranges (0.95–2.2 THz, 4.15–5.4 THz, and 7.3–8.55 THz), and the total tunable frequency range reaches 3.75 THz. The maximum absorption of the LCP wave can reach 99.91% due to the destructive interference of the reflected waves and the graphene-induced photonic band gap. In addition, the influence of the incident angle on magnetic tuning is also analysed. The perfect absorption of the LCP wave at the absorption peak frequency is unaffected when the incident angle is less than 40°. Finally, the influence of the loss of the nonmagnetic dielectric SiO_2 on the magnetically tunable absorption performance is investigated. It is shown that a more stable magnetically tunable absorption performance can be achieved in practice when the extinction coefficient of the nonmagnetic dielectric SiO_2 $\kappa_{sio_2} \leq 0.001$. This study provides a new concept for magnetically tunable THz perfect absorbers over a wide frequency range, which have potential applications in various fields such as detectors, sensors, and other optoelectronic devices.

Author Contributions: Conceptualization, Y.J.; writing—original draft preparation, Z.W.; validation, J.W.; writing—review and editing, Z.W., Y.J. and J.W. All authors have read and agreed to the published version of the manuscript.

Funding: This work was supported by the National Natural Science Foundation of China (Grant No. 62261015), Natural Science Foundation of Guangxi Province (Grant No. 2019GXNSFFA245002), Dean Project of Guangxi Key Laboratory of Wireless Wideband Communication and Signal Processing (Grant No. GXKL06190114), and Middle-aged and Young Teachers' Basic Ability Promotion Project of Guangxi (Grant No. 2020KY05028).

Data Availability Statement: The data supporting the results of this study are available from the corresponding author upon reasonable request.

Acknowledgments: The authors acknowledge the support from the School of Information and Communication, Guilin University of Electronic Technology.

Conflicts of Interest: The authors declare no conflict of interest.

References

1. Tse, W.K.; Qiao, Z.; Yao, Y.; MacDonald, A.; Niu, Q. Quantum anomalous Hall effect in single-layer and bilayer graphene. *Phys. Rev. B* **2011**, *83*, 155447. [CrossRef]
2. Yi, Z.; Liu, L.; Wang, L.; Cen, C.; Chen, X.; Zhou, Z.; Ye, X.; Yi, Y.; Tang, Y.; Yi, Y.; et al. Tunable dual-band perfect absorber consisting of periodic cross-cross monolayer graphene arrays. *Results Phys.* **2019**, *13*, 102217. [CrossRef]
3. Grigorenko, A.N.; Polini, M.; Novoselov, K. Graphene plasmonics. *Nat. Photonics* **2012**, *6*, 749–758. [CrossRef]
4. Weis, P.; Garcia-Pomar, J.L.; Hoh, M.; Reinhard, B.; Brodyanski, A.; Rahm, M. Spectrally wide-band terahertz wave modulator based on optically tuned graphene. *ACS Nano* **2012**, *6*, 9118–9124. [CrossRef]
5. Zhang, D.; Zhang, L. Tunable terahertz dual-band band-stop filter based on surface magnetoplasmons in graphene sheet array. *Opt. Laser Technol.* **2020**, *132*, 106484. [CrossRef]
6. Chen, M.; Zhang, W.; Deng, S.; Liu, H.; Teng, C.; Deng, H.; Yang, H.; Xu, R.; Yin, J.; Yu, L.; et al. Wide-range frequency tunable absorber based on cross-groove metamaterials and graphene-sheet. *J. Phys. D Appl. Phys.* **2020**, *53*, 255102. [CrossRef]
7. Zaky, Z.A.; Al-Dossari, M.; Zohny, E.I.; Aly, A.H. Refractive index sensor using Fibonacci sequence of gyroidal graphene and porous silicon based on Tamm plasmon polariton. *Opt. Quantum Electron.* **2023**, *55*, 6. [CrossRef]
8. Zaky, Z.A.; Singh, M.R.; Aly, A.H. Tamm resonance excited by different metals/graphene. *Photonics Nanostruc.* **2022**, *49*, 100995. [CrossRef]
9. Zaky, Z.A.; Aly, A.H. Gyroidal graphene/porous silicon array for exciting optical Tamm state as optical sensor. *Sci. Rep.* **2021**, *11*, 19389. [CrossRef]
10. Zaky, Z.A.; Sharma, A.; Aly, A.H. Gyroidal graphene for exciting tamm plasmon polariton as refractive index sensor: Theoretical study. *Opt. Mater.* **2021**, *122*, 111684. [CrossRef]
11. Divdel, H.; Taghipour-Farshi, H.; Saghai, H.R.; Jahani, M.A.T.G. Thermally switchable terahertz metasurface absorber composed of H-fractal and enabled by phase-change material of vanadium dioxide. *Frequenz* **2022**, *76*, 169–175. [CrossRef]
12. Butt, M.; Khonina, S.; Kazanskiy, N.; Piramidowicz, R. Hybrid metasurface perfect absorbers for temperature and biosensing applications. *Opt. Mater.* **2022**, *123*, 111906. [CrossRef]
13. Chung, M.; Jeong, H.; Kim, Y.K.; Lim, S.; Baek, C.W. Design and Fabrication of Millimeter-Wave Frequency-Tunable Metamaterial Absorber Using MEMS Cantilever Actuators. *Micromachines* **2022**, *13*, 1354. [CrossRef] [PubMed]
14. Bilal, R.; Baqir, M.; Iftikhar, A.; Naqvi, S.; Mughal, M.; Ali, M. Polarization-controllable and angle-insensitive multiband Yagi-Uda-shaped metamaterial absorber in the microwave regime. *Opt. Mater. Express* **2022**, *12*, 798–810. [CrossRef]
15. Jornet, J.M.; Akyildiz, I.F. Channel modeling and capacity analysis for electromagnetic wireless nanonetworks in the terahertz band. *IEEE Trans. Wireless Commun.* **2011**, *10*, 3211–3221. [CrossRef]
16. Koppens, F.H.; Chang, D.E.; García de Abajo, F.J. Graphene plasmonics: A platform for strong light–matter interactions. *Nano Lett.* **2011**, *11*, 3370–3377. [CrossRef]
17. Rashidi, A.; Namdar, A.; Abdi-Ghaleh, R. Magnetically tunable enhanced absorption of circularly polarized light in graphene-based 1D photonic crystals. *Appl. Opt.* **2017**, *56*, 5914–5919. [CrossRef]
18. Jin, X.; Wang, F.; Huang, S.; Xie, Z.; Li, L.; Han, X.; Chen, H.; Zhou, H. Coherent perfect absorber with independently tunable frequency based on multilayer graphene. *Opt. Commun.* **2019**, *446*, 44–50. [CrossRef]

19. Yi, Z.; Chen, J.; Cen, C.; Chen, X.; Zhou, Z.; Tang, Y.; Ye, X.; Xiao, S.; Luo, W.; Wu, P. Tunable graphene-based plasmonic perfect metamaterial absorber in the THz region. *Micromachines* **2019**, *10*, 194. [CrossRef]
20. Zhang, B.; Qi, Y.; Zhang, T.; Zhang, Y.; Liu, W.; Wang, L.; Ding, J.; Wang, X.; Yi, Z. Tunable multi-band terahertz absorber based on composite graphene structures with square ring and Jerusalem cross. *Results Phys.* **2021**, *25*, 104233. [CrossRef]
21. Norouzi-Razani, A.; Rezaei, P. Multiband polarization insensitive and tunable terahertz metamaterial perfect absorber based on the heterogeneous structure of graphene. *Opt. Quantum Electron.* **2022**, *54*, 407. [CrossRef]
22. Fu, P.; Liu, F.; Ren, G.J.; Su, F.; Li, D.; Yao, J.Q. A broadband metamaterial absorber based on multi-layer graphene in the terahertz region. *Opt. Commun.* **2018**, *417*, 62–66. [CrossRef]
23. Ye, L.; Zeng, F.; Zhang, Y.; Xu, X.; Yang, X.; Liu, Q.H. Frequency-reconfigurable wide-angle terahertz absorbers using single-and double-layer decussate graphene ribbon arrays. *Nanomaterials* **2018**, *8*, 834. [CrossRef]
24. Gong, J.; Shi, X.; Lu, Y.; Hu, F.; Zong, R.; Li, G. Dynamically tunable triple-band terahertz perfect absorber based on graphene metasurface. *Superlattices Microstruct.* **2021**, *150*, 106797. [CrossRef]
25. Mou, N.; Sun, S.; Dong, H.; Dong, S.; He, Q.; Zhou, L.; Zhang, L. Hybridization-induced broadband terahertz wave absorption with graphene metasurfaces. *Opt. Express* **2018**, *26*, 11728–11736. [CrossRef]
26. Kumar, P.; Lakhtakia, A.; Jain, P.K. Graphene pixel-based polarization-insensitive metasurface for almost perfect and wideband terahertz absorption. *JOSA B* **2019**, *36*, F84–F88. [CrossRef]
27. Kong, X.K.; Shi, X.Z.; Mo, J.J.; Fang, Y.T.; Chen, X.L.; Liu, S.B. Tunable multichannel absorber composed of graphene and doped periodic structures. *Opt. Commun.* **2017**, *383*, 391–396. [CrossRef]
28. Wang, X.; Jiang, X.; You, Q.; Guo, J.; Dai, X.; Xiang, Y. Tunable and multichannel terahertz perfect absorber due to Tamm surface plasmons with graphene. *Photonics Res.* **2017**, *5*, 536–542. [CrossRef]
29. Bian, L.A.; Deng, Z.; Hong, Y.; Qiu, Y.; Liu, Z.; Xiao, P.; Li, G. Double-mode absorption in double-defect photonic crystal with one graphene multilayer. *Opt. Quantum Electron.* **2020**, *52*, 1–10. [CrossRef]
30. Wei, Z.; Jiang, Y.; Zhang, S.; Zhu, X.; Li, Q. Graphene-Based Magnetically Tunable Broadband Terahertz Absorber. *IEEE Photonics J.* **2021**, *14*, 1–6. [CrossRef]
31. Cheng, R.; Zhou, Y.; Liu, H.; Liu, J.; Sun, G.; Zhou, X.; Shen, H.; Wang, Q.; Zha, Y. Tunable graphene-based terahertz absorber via an external magnetic field. *Opt. Mater. Express* **2020**, *10*, 501–512. [CrossRef]
32. Rashidi, A.; Nayak, C.; Bezerra, C.G.; Costa, C.H.; Pinheiro, F.A. Tunable terahertz absorption in Si/SiO_2-graphene multilayers: Disorder and magneto-optical effects. *Appl. Opt.* **2020**, *59*, 11034–11040. [CrossRef] [PubMed]
33. Entezar, S.R.; Habil, M.K. Nonreciprocal optical isolation via graphene based photonic crystals. *J. Magn. Magn. Mater.* **2018**, *449*, 33–39. [CrossRef]
34. Mahesh, P.; Nayak, C. Multimode absorption in single-layer graphene: Disordered photonics and magneto-optic effect. *Opt. Mater.* **2022**, *126*, 112172. [CrossRef]
35. Crassee, I.; Levallois, J.; Walter, A.L.; Ostler, M.; Bostwick, A.; Rotenberg, E.; Seyller, T.; Van Der Marel, D.; Kuzmenko, A.B. Giant Faraday rotation in single-and multilayer graphene. *Nat. Phys.* **2011**, *7*, 48–51. [CrossRef]
36. Lin, X.; Wang, Z.; Gao, F.; Zhang, B.; Chen, H. Atomically thin nonreciprocal optical isolation. *Sci. Rep.* **2014**, *4*, 1–5. [CrossRef] [PubMed]
37. Berreman, D.W. Optics in stratified and anisotropic media: 4× 4-matrix formulation. *Josa* **1972**, *62*, 502–510. [CrossRef]
38. Molina, I.; Adrián Reyes, J.; Avendaño, C.G. Electrically controlled optical bandgap in a twisted photonic liquid crystal. *J. Appl. Phys.* **2011**, *109*, 113510. [CrossRef]
39. Habil, M.K.; Entezar, S.R. Polarization conversion and phase modulation of terahertz electromagnetic waves via graphene-dielectric structure. *Phys. Scr.* **2019**, *95*, 015503. [CrossRef]
40. Hung, H.C.; Wu, C.J.; Chang, S.J. Terahertz temperature-dependent defect mode in a semiconductor-dielectric photonic crystal. *J. Appl. Phys.* **2011**, *110*, 093110. [CrossRef]
41. Wang, X.; Zhao, M.; Nolte, D.D. Optical contrast and clarity of graphene on an arbitrary substrate. *Appl. Phys. Lett.* **2009**, *95*, 081102. [CrossRef]
42. Stephens, P.J. Magnetic circular dichroism. *Annu. Rev. Phys. Chem.* **1974**, *25*, 201–232. [CrossRef]
43. Wang, W.; Qu, Y.; Du, K.; Bai, S.; Tian, J.; Pan, M.; Ye, H.; Qiu, M.; Li, Q. Broadband optical absorption based on single-sized metal-dielectric-metal plasmonic nanostructures with high-ε'' metals. *Appl. Phys. Lett.* **2017**, *110*, 101101. [CrossRef]
44. Madani, A.; Entezar, S.R. Optical properties of one-dimensional photonic crystals containing graphene sheets. *Phys. B* **2013**, *431*, 1–5. [CrossRef]
45. Kim, T.T.; Oh, S.S.; Kim, H.D.; Park, H.S.; Hess, O.; Min, B.; Zhang, S. Electrical access to critical coupling of circularly polarized waves in graphene chiral metamaterials. *Sci. Adv.* **2017**, *3*, e1701377. [CrossRef]
46. Qi, L.; Liu, C. Complex band structures of 1D anisotropic graphene photonic crystal. *Photonics Res.* **2017**, *5*, 543–551.

Disclaimer/Publisher's Note: The statements, opinions and data contained in all publications are solely those of the individual author(s) and contributor(s) and not of MDPI and/or the editor(s). MDPI and/or the editor(s) disclaim responsibility for any injury to people or property resulting from any ideas, methods, instructions or products referred to in the content.